### **Research Article**

Mohammed Raed Rasheed\* and Shatha Dheyaa Mohammed

# Structural behavior of one-way slabs reinforced by a combination of GFRP and steel bars: An experimental and numerical investigation

https://doi.org/10.1515/jmbm-2024-0002 received November 14, 2023; accepted March 15, 2024

Abstract: Glass- fiber-reinforced polymer (GFRP) offers a significant alternative to steel in reinforced concrete, with superior corrosion and fire resistance. Though less ductile and more brittle in stress-strain behavior than steel, it is very helpful to combine GFRP with steel reinforcement that improves the structural behavior. This research investigates the flexural characteristics of a one-way slab reinforced by a combination of GFRP and steel reinforcement. Three identical concrete slabs ((1500  $\times$  550  $\times$  120) mm and 43 MPa) were tested under static load with GFRP replacement ratios of (0, 20, and 40)%. The experimental data were utilized to verify a numerical model. The experimental outcomes indicated a substantial impact of the GFRP replacement ratio on the failure mode. The failure mode was flexural, flexural-shear, and shear regarding the reference slab, 20%, and 40% replacement, respectively. GFRP replacement influenced ductility and ultimate load by (9.13 and 10.7)% and (-21 and 5.0)% for replacement ratio (20 and 40)%, respectively. Based on the numerical analysis, the parametric study (considerably affected the structural response. Failure mode changed to flexural, and shear-flexural concerning (20 and 40)%, respectively. The optimum load was characterized at 40%, while max toughness and ductility were achieved at 20%.

**Keywords:** GFRP bars, one-way slab, ductility, flexural resistance, finite element, compressive strength

### 1 Introduction

In the latter part of the twentieth century, there was a significant expansion in the use of glass fiber-reinforced polymer (GFRP) composites to enhance the strength of reinforced concrete structures. This technology has shown a great potential in addressing the rehabilitation needs of various infrastructures. GFRP strengthening has been used in many applications, including constructing new buildings and rehabilitating of existing structures [1–3]. In addition to studying the global failure criteria of GFRP with reinforced concrete (RC) elements, many researchers have concentrated on studying the localized failure mode, *i.e.*, the bond interface strength and support failure [4].

Within the range of fiber-reinforced polymers (FRPs), GFRP was recommenced in reinforced concrete technology due to its ability to minimize corrosion-related problems compared to steel bars [5-9]. Consequently, using GFRP bars has seen a growing trend in their application as embedded concrete reinforcement. This may be attributed to their advantageous characteristics, including their low weight, high tensile strength, and resistance to corrosion [10,11]. Nevertheless, the characteristics of these materials are determined mainly by many parameters, including the fiber's kind, fiber's orientation, fiber's proportional volume, the type of used resin, and the level of quality control implemented throughout the production process. Generally, fiber volume refers to the number of fibers in a unit area of GFRP cross-section. Moreover, the level of quality control implemented is crucial in determining the overall quality and performance of the GFRP materials, contributing to their mechanical strength, stiffness, and longterm durability [11]. GFRP bars demonstrate linear elastic characteristics and brittleness, revealing a reduced level of ductility compared to steel bars. This may be attributed to the lower tensile modulus of elasticity present in GFRP bars [12].

GFRP bars can replace steel bars; however, their quantity and arrangement must be optimized. This optimization

<sup>\*</sup> Corresponding author: Mohammed Raed Rasheed, Civil Engineering Department, University of Baghdad, Baghdad, Iraq, e-mail: mohammed.raed2101m@coeng.uobaghdad.edu.iq

Shatha Dheyaa Mohammed: Civil Engineering Department, University of Baghdad, Baghdad, Iraq, e-mail: shatha.dh@coeng.uobaghdad.edu.iq

process must ensure that the structural element can restore strength after deformation or stress and does not prevent steel bars from yielding (causing a brittle failure). Another objective is to optimize the GFRP bar amount and the arrangement for maximum load-bearing capacity. Placement or layout within the structure is called "arrangement." The sentence implies that the quantity and distribution of GFRP bars in a structure affect their performance. Furthermore, it is vital to consider the elastic deflection observed in the structure as the load increases [13].

Nevertheless, it is worth noting that concrete slabs reinforced with FRP bars sometimes demonstrate abrupt brittle failure. As a result, researchers have investigated the efficacy of hybrid reinforced concrete buildings, which integrate the advantages of FRP and steel bars [14–17]. Previous research has examined the use of GFRP bars as a feasible alternative to conventional steel reinforcement in concrete elements, aiming to address the issues associated with corrosion and structural degradation of steel reinforcement. The reduced modulus of elasticity and lack of yielding behavior shown by (FRP) materials result in significant deflection and broad cracks in concrete components reinforced with GFRP. Therefore, it is essential to use an appropriate design approach and techniques to evaluate this behavior precisely [16].

Chang and Seo [18] examined the structural performance of reinforced concrete blocks with GFRP bars as reinforcement when only one point held them. The measurements of the slabs were as follows:  $4,000 \times 1,000 \times 150$ mm and 4,000 × 1,000 × 200 mm, and their reinforcing ratios varied. The investigated goal was to examine the slabs' flexural and shear limit states, covering parameters such as behavior before breaking, cracking pattern and breadth, deflections, ultimate strength, and failure processes. The results show that the GFRP-reinforced blocks that were studied followed a bilinear elastic pattern until they broke. Given that FRP deforms linear elastically and that concrete crushing often determines the failure mechanism of FRP-reinforced slabs. When cracks appeared, the slabs reinforced with GFRP bars were significantly less stiff than slabs reinforced with steel. To control displacement effectively, increasing the reinforcement ratios to provide sufficient bending stiffness is important.

Sadraie *et al.* [19] conducted a comprehensive investigation on the impact of various factors, including the material composition of rebar, the quantity and arrangement of reinforcements, and the slab thickness on the dynamic behavior of reinforced concrete slabs. This study used a combination of laboratory tests and numerical simulations to analyze the variables mentioned above. The experimental investigation focused on performing 15 concrete

slabs of 1,000  $\times$  1,000 mm. These slabs were reinforced with GFRP bars, while two slabs were reinforced with steel bars. The specimens underwent finite element analysis (FEA) and simulations using the LS-DYNA explicit program. The findings derived from both experimental investigations and numerical simulations demonstrate a high level of concurrence. It has been observed that by appropriately modifying the quantity and configuration of GFRP, superior performance can be obtained in GFRP slabs compared to slabs reinforced with steel. This advantage, coupled with the corrosion resistance exhibited by GFRP, renders it a suitable choice for reinforcement material.

Al-Rubaye *et al.* [20] evaluated the flexural performance of concrete slabs reinforced with GFRP bars and a composite reinforcing system. Four concrete slabs were carefully manufactured and subsequently underwent thorough testing to gain insights into the performance features of this innovative construction method. Carbon-reinforced polymer (CRP) has been observed to enhance the structural stability of hollow concrete slabs. The increased compatibility between CRP and GFRP bars, in comparison to steel bars, is due to their similar modulus of elasticity. The precise estimation of the load-bearing capacity of hollow concrete slabs was achieved through the utilization of a simplified fiber model analysis.

Adam *et al.* [21] investigated the structural performance of a high-strength concrete slab reinforced with locally made fiber-reinforced polymer. Following that, a finite element (FE) model was created using ANSYS 2019-R1 and validated with the experimental data. The results showed that using GFRP bars in concrete slabs improved ductility and increased deflection when compared to the standard steel bars. The experimental results and FE computations agreed highly.

The flexural performance of concrete slabs with apertures reinforced by GFRP bars and enhanced using carbon fiber-reinforced polymer (CFRP) sheets was studied by Golham and Al-Ahmed [22]. Five distinct concrete slabs were tested in a one-way layout as part of the experimental investigation up to the point of collapse. A specimen that resembled a solid slab and was free of reinforcement and holes was used in the experimental investigation. The remaining slabs had CFRP sheets added for reinforcement and were made with rectangular and square openings, respectively. According to the experimental results, until they failed, the slabs reinforced with GFRP behaved in a manner that was bilinear elastic. The slabs' rigidity was noticeably reduced as the fractures started to appear. Compared to a solid slab in the final stage, slabs with one hole had a stiffness loss of around 23%, while slabs with two apertures showed a fall of about 31%. In addition, an FE

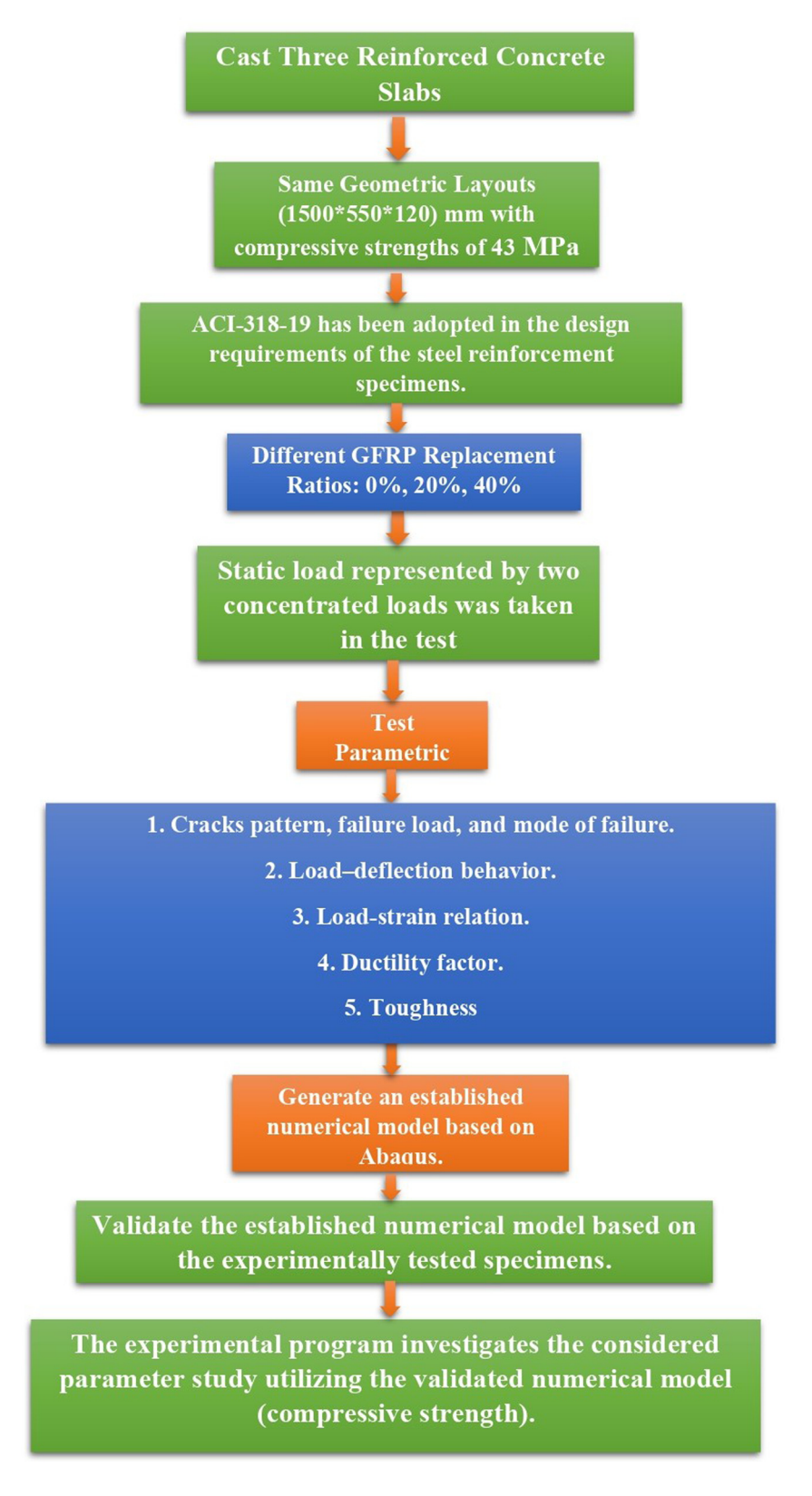


Figure 1: Flowchart for the research methodology.

model was verified using the empirical data in combination with a separate parametric analysis.

According to the outcomes of the literature review, FRP deforms linearly elastically because the crushing of concrete frequently determines the failure mechanism of FRP-reinforced slabs. The decision to use hybrid reinforcement a combination of steel and GFRP bars was made intentionally to leverage the distinct qualities of each material. Steel provides strong tensile strength and ductility, while GFRP bars have advantages like corrosion resistance, lightweight characteristics, and a high strength-to-weight ratio. This comprehensive approach aims to maximize the benefits of both materials, ultimately leading to superior. There has been little research on the structural effect of utilizing GFRP bars in conjunction with steel bars. As a result, this research aims to perform experimental studies on the structural behavior of reinforced concrete one-way slabs using GFRP bars in combination with steel bars. The GFRP replacement percentages were 0, 20, and 40%. The testing findings were examined, and they covered the initial cracking load, ultimate load-deflection behavior, ductility, and toughness. Furthermore, the experimental data were utilized to evaluate a finite element model alongside a parametric investigation of the concrete compressive strength effect.

# 2 Research significance

With a focus on their reaction to flexural pressures, the study aims to evaluate the structural performance of using GFRP bars in place of steel bars. In addition, this study aims to offer validated nonlinear finite element simulations as a suggestion for precisely projecting the structural behavior of steel rods and GFRP one-way slabs. The process of this study's methodology is depicted in a flowchart in Figure 1.

Table 1: Cement chemical composition

#### Compound composition **Chemical composition** Content (%) Limit of Iraqi Specification No. 5/2019 L.O. I 3.63 ≤4% Loss on ignition Insoluble material I.R. 0.58 ≤1.5% Sulfate $SO_3$ 2.35 ≤2.8% Chloride 0.02 ≤0.1% Tricalcium aluminate СЗА 4.68 1.83 <5% Magnesia MgO

# 3 The experimental program

### 3.1 Constitutive materials

### 3.1.1 Cement

All the experimental samples and the control specimens were cast using ordinary Portland cement (CEM I 42.5R) from the (Mass) brand within Iraq. The outcomes of the chemical tests are presented in Table 1 and the physical tests in Table 2. The results of the cement testing met the requirements of Iraqi Specification No. 5/2019 [23].

### 3.1.2 Fine aggregate and coarse aggregate

The maximum size of the crushed gravel siliceous aggregate used in the investigation was 12 mm. Aggregates, both fine and coarse, showed compliance with the Iraqi Specification (IQS) No. 45/1984 and subsequent updates [24]. In accordance with the parameters of Iraqi Specification No. 45/1984 and its amendments [24], the test results are displayed in Tables 3 and 4.

### 3.1.3 Additive material

A chemical additive was added to achieve the desired strength of the concrete mix. This additive increased compressive strength while maintaining workability without using extra water amount. This is crucial, as excessive water leads to weakened concrete and reduced strength due to the evaporation of excess water over time from the heat of the cement-water reaction, leaving voids in the concrete mixture. Therefore, Sika's superplasticizer (CHRYSO®Optima 100) was utilized. Table 5 shows the properties of the used plasticizer.

Table 2: Cement physical composition

Physical properties	Test results	Limit of Iraqi Specification No. 5/2019
Specific surface area (Blaine method), (m²/kg)	346	≥250
Setting time (Vicat's method)		
Initial setting time ( min)	148	≥45 min
Final setting time (min)	195	≤600 min
Compressive strength (MPa)		
For 2-day	23.7	≥10 MPa
For 28-day	45	≥42.5 MPa

Table 3: Fine aggregate properties

	Sieve	Dry w	eight (g)	Cumulative passing (%)	Limit of the Iraqi Specification No. 45/1		Limit of the Iraqi Specification No. 45/1984	
mm	Mesh	Ret	aining		Zone 1	Zone 2	Zone 3	Zone 4
		g	%					
9.5	3/8 in	0.0	0.0	100	100-100	100–100	100-100	100-100
4.75	No. 4	77.0	7.0	94	90-100	90-100	90-100	90-100
2.36	No. 6	239	21.8	78	60-95	75-100	85-100	95-100
1.18	No .16	412	37.6	60	30-70	55-90	75-100	90-100
0.60	No. 30	708	64.5	37	15-34	35-59	60-79	80-100
0.30	No. 50	990	90.2	19	5–20	8-30	12-40	15-50
0.15	No. 100)	1077	98.2	3.4	0–10	0–10	0-10	0-15
0.075	No. 200	1093	99.6	0.4	0–5	0-5	0-5	0-5
Finen	ess modulus	3.19						
1	Specific gravity	2.67			_			
2	Sulfate content (SO <sub>3</sub> )(%)	0.05			0.5	(max.)		
3	Absorption %	1.05						

### 3.1.4 Steel reinforcement

Steel bars of deformed shape were considered for longitudinal and transverse of 10 and 8 mm, respectively. The properties of reinforced bars are listed in Table 6. One piece of 1,000 mm in length for each diameter was tested, and the results were identical to ASTM A615M [25]. The

Table 4: Coarse aggregate properties

Sieve size (mm)	Passing (%)			
	Coarse aggregate	Iraqi specification No. 45/1984		
20	95.19	95–100		
10	31.646	30-60		
4.75	2.025	0–10		
Specific gravity	2.659	_		
Sulfate content (SO <sub>3</sub> )(%)	0.046	<0.5%		
Absorption	0.846			

specimen was tested under direct tension in the Consulting Engineering Bureau/College of Engineering/University of Baghdad. The grade of steel is 60.

### 3.1.5 GFRP reinforcement

GFRP bars were used in the tension zone only for longitudinal reinforcement of (10 mm) diameter. The properties of GFRP bars are listed in Table 7. The used GFRP bars were manufactured by a factory in Iran, and the tests were conducted in Iran in the laboratory (Razi Metallurgical Center).

### 3.1.6 Mix design

Table 8 displays the mixture specifications used to attain the certified compressive strength of  $f_{cu}$  = 54 MPa, designed by Lafarge Ready Mix Company.

Table 5: Technical properties of superplasticizer

Indicative information	
Product nature	Liquid
Color	Translucent yellow
Lifetime	9 months
Freezing point	3°C
Specifications	
Halogen dry extract	$30.20 \pm 1.50\%$
CI- lons content	≤0.100%
Equivalent content NA <sub>2</sub> O	≤0.30%
Specific gravity (20°C) (kg/dm³)	$1.061 \pm 0.020$
pH (2°C)	$4.70 \pm 1.00$
Dry extract (EN 480-8)	31.00 ± 1.500%

### 3.2 Tested specimens

Three identical concrete slabs of the same geometric design and concrete mix portion were tested as part of the experimental program for this investigation. ACI-318-19 [26] standards for design requirements for steel reinforcement in specimens have been adopted. The dimensions of each slab were  $1,500 \times 550 \times 120$  mm. Figures 2 and 3 and Table 9 summarize further information about the test specimens.

## 3.3 Testing procedures

The slabs were mounted to two hemispherical supports, specifically designed to provide simple support. At the

mid-span of all slab specimens, strain gauges with a gauge length of 60 mm were fastened to the concrete compression face. Figure 5 depicts the strain gauges positions (concrete). The distance between the supports was measured to be 1,300 mm, which corresponds to the length of the slabs under investigation. A hydraulic jack with a capacity of 100 tons was then employed to apply the static load. This load was distributed evenly by a steel loading I-section girder, resulting in two equal forces separated by a span of 400 mm. Throughout the experiment, various measurements were recorded, including the applied load amplitude, vertical deflection at the center of the slab, and strain experienced by the steel reinforcement, GFRP reinforcement, and concrete surface (Figures 4 and 5). These measurements were recorded at each step of the loading process. The load was incrementally increased until the failure stage, each step consisting of a 2.5 kN increase. The development of cracks was carefully observed and documented after each increment. Figures 5 and 6 comprised more comprehensive details of the experimental setup.

The adjusted load increment before crack generation was small, so it enabled the crack load to be traced. After each increment, checking for all surfaces of the specimen was included to ensure there was no crack generated. As the cracks were generated, load steps were increased to 5 kN until the failure stage. Moreover, the measured crack load in the experimental test was checked with the load–deflection disposition since the slope of the load–deflection curve is reduced as the crack is generated (Figure 7).

Table 6: Properties of steel reinforcement

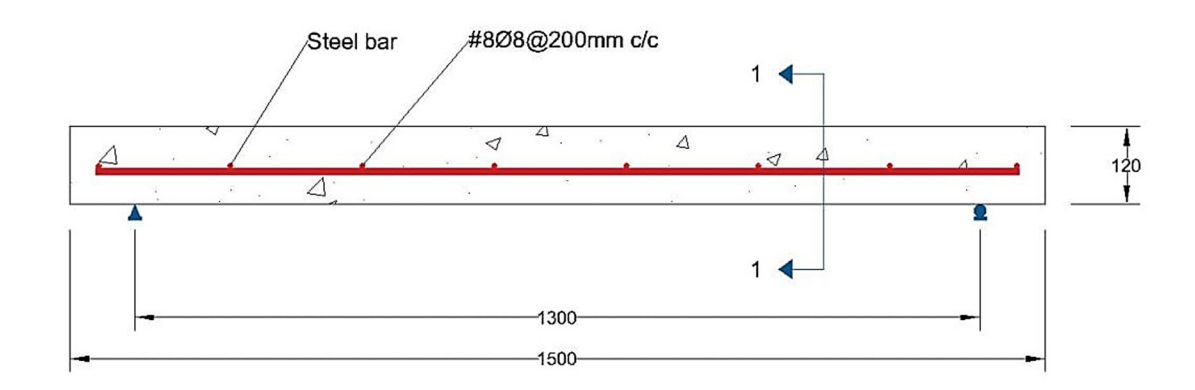
Bars type	Nominal diameter (mm)	Yield stress (MPa)	Ultimate strength (MPa)	Modulus of elasticity <i>E</i> (MPa)	Elongation (%)
Steel	10	437	527	200,000	11
Steel	8	434	483	200,000	12

Table 7: Properties of GFRP Reinforcement

Nominal bar diameter (mm)	As (mm²)	Tensile strength (MPa)	Elongation (%)	Modulus of elasticity (MPa)	Density (kg/m³)
10	78.5	1207	2.5	48,280	2,084

Table 8: Details of concrete mix proportions

Cement (kg/m³)	Gravel (kg/m³)	Sand (kg/m³)	Water (L/m³)	Optima 100 (kg/m³)	Silica fume (kg/m³)	Splitting strength $f_{ m t}$ (MPa)	Specimen strength $f_{ m cu}$ (MPa)
470	945	827	170	6.2	20	3.56	54



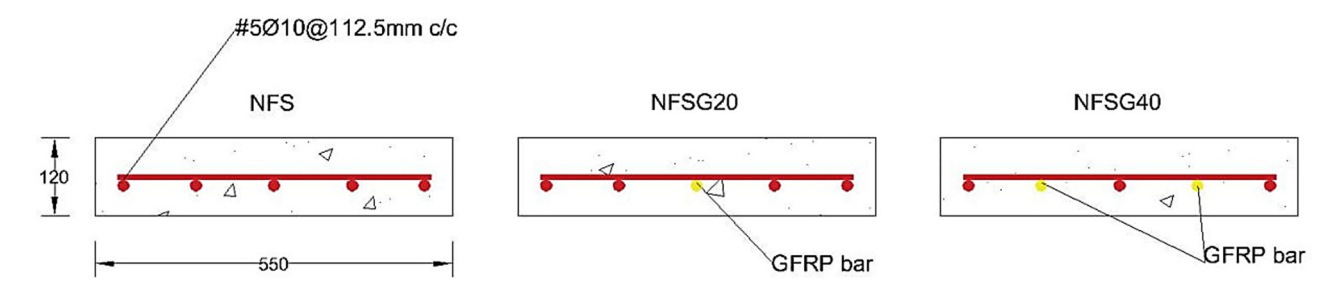


Figure 2: Dimensions and reinforcement information of the tested specimens (dimensions: mm).

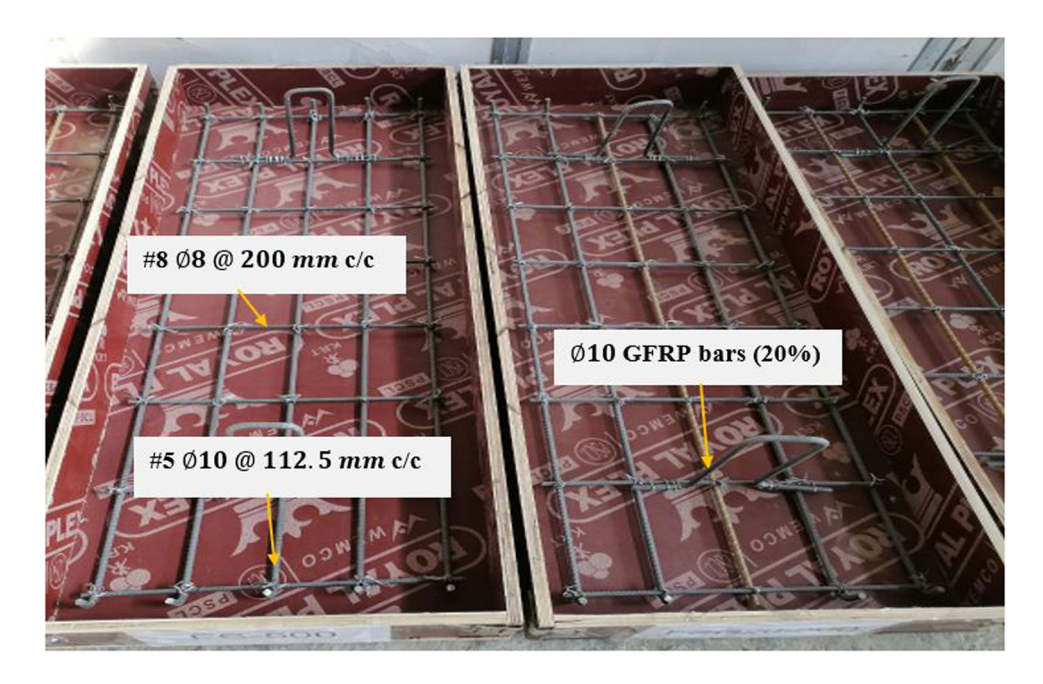


Figure 3: Details of the adopted reinforcement combination.

# 4 Test results and discussions

Three reinforced concrete slabs with various ratios of GFRP bars in place of steel bars were put to the test when a two-point load was applied. Up to the point of

failure, the load was gradually raised. Four categories were used in the discussion of the data to understand the structural behavior of the slab better.

- 1. Cracks pattern, failure load, and mode of failure.
- 2. Load-deflection behavior.

Table 9: Characteristics of the tested specimens

NO	Slab Designation	$f_{ m c}^{\prime}$ (MPa)	GFRP bars in place of steel bars
1	NFS	43	0
2	NFSG20	43	20
3	NFSG40	43	40

- 3. Load-strain relation.
- 4. Ductility factor.
- 5. Toughness.

# 4.1 Cracks pattern, failure load, and mode of failure

The experimental results regarding the cracking loads and the failure loads are listed in Table 10. Regarding the first flexural crack, GFRP bars had a significant effect on the cracking load reduction. The replacement percentage increase of steel bars by GFRP bars decreased the cracking load by about 6.3 and 21% for the replacement of 20 and 40% concerning the reference specimen (0% replacement). The deterioration in the crack load is mainly caused by the specimen stiffness reduction that belongs to the low modulus of

elasticity for the GFRP compared to that of the steel. The first flexural fracture manifested at the central region of the slab tension face, maximum moment location, as the tensile stresses in the lowermost concrete fiber surpassed the modulus of rupture of the concrete. Subsequently, fractures gradually formed around the periphery of the slabs, running parallel to the direction of the support.

Regarding the reference slab (NFS), when the applied load was increased, flexural cracks were generated and propagated on the bottom surface of the slab. These cracks were seen to be parallel to the original fracture and aligned with the direction of the supports. Subsequently, the fractures underwent propagation toward the lateral edges of the slab, ultimately reaching the compression zone of the slab at the failure phase. The presence of fractures in the slab's central portion was apparent, whereas no cracks were detected in the support vicinity. In addition, it was noted that there were no instances of shear fractures being formed. The cracking pattern of the failure stage is shown in Figure 8.

Concerning the slab (NFSG40), with a replacement of 40%, the crack pattern was completely different. As the applied load continued to grow, flexural cracks were generated and propagated along the bottom surface of the slab. The cracks were running parallel to both the original fracture and

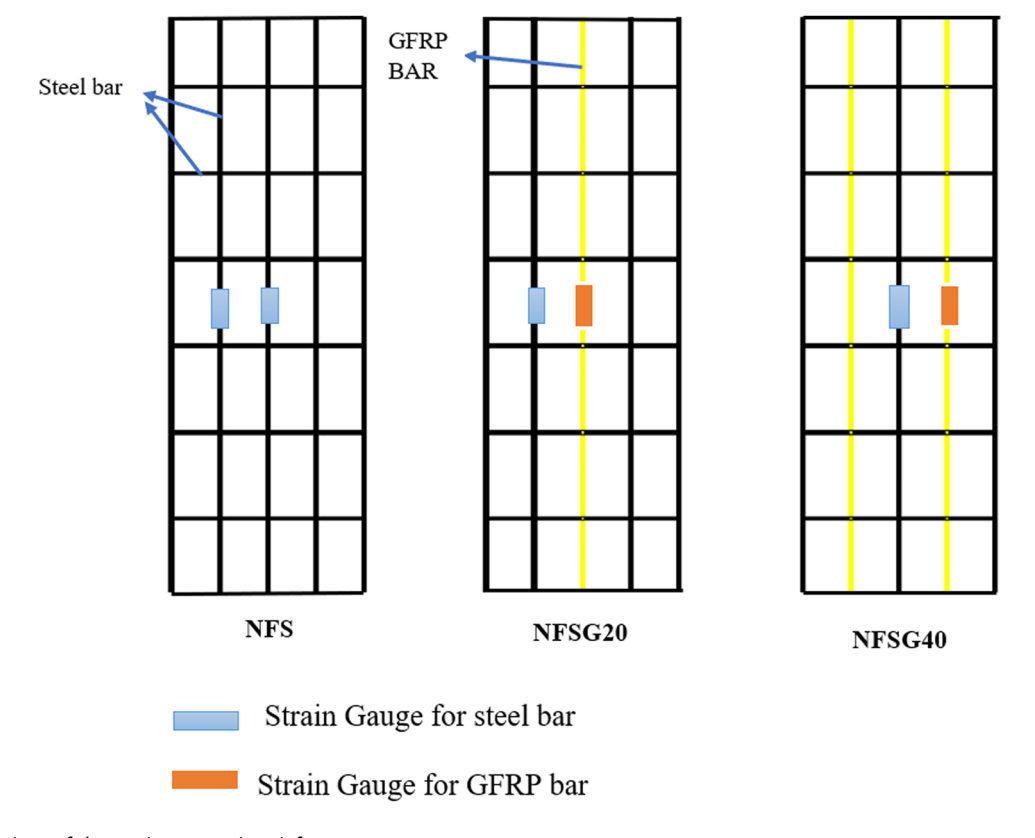


Figure 4: Locations of the strain gauges in reinforcement.

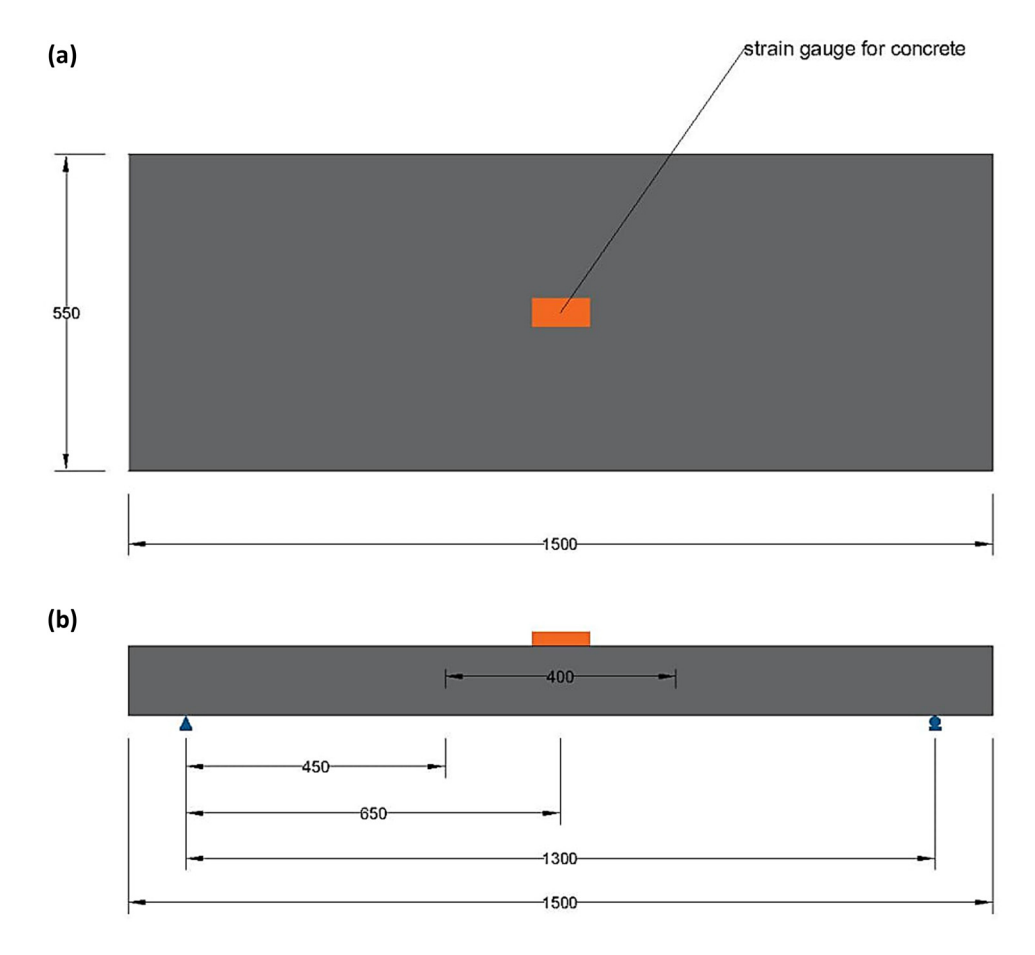


Figure 5: Locations of the strain gauge: (a) top face and (b) side face (dimensions: mm).

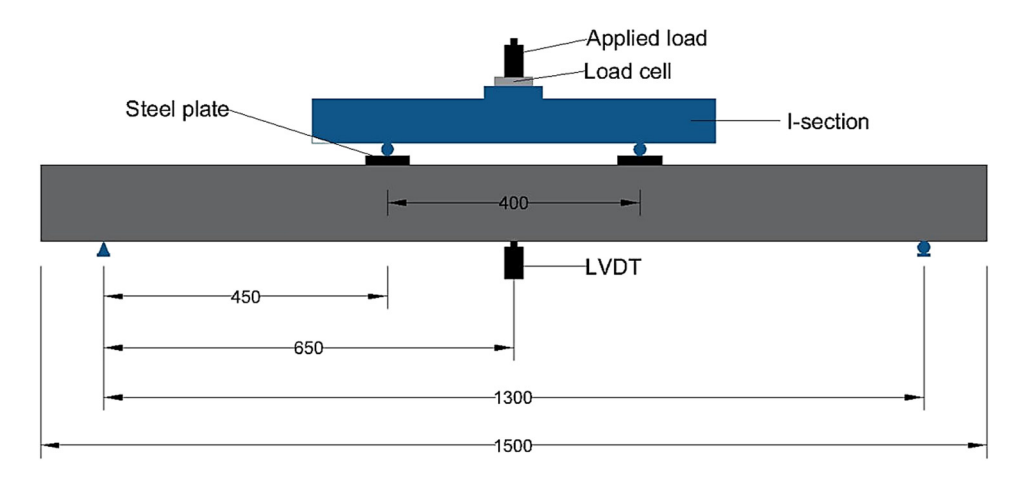


Figure 6: Details of the test setup (dimensions: mm).

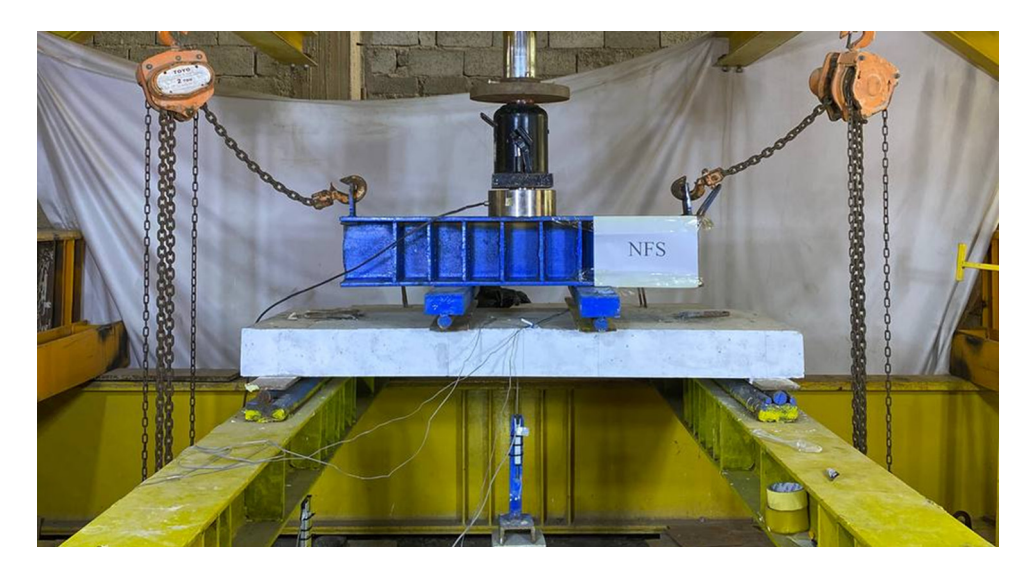


Figure 7: Test setup.

Table 10: Cracking and ultimate loads of the tested specimens

Specimens	Ultimate load $P_{ m u}$ (kN)	% Increase in relation to Ref.	Cracking load $P_{ m cr}$ (kN)	% Decrease in $P_{ m cr}$ with respect to Ref.	$P_{\rm cr}/P_{\rm u}$ (%)
NFS	79.62	Ref.	19	Ref.	24
NFSG20	88.13	10.7	17.8	6.3	20
NFSG40	83.64	5	15	21	18

the direction of the supports. Subsequently, the slab experienced the propagation of diagonal shear fractures toward its lateral edges at Load (77 kN). As the applied Load progressively increased, the shear fractures tended to spread in an upward direction inside the slab, moving toward the loading location. The slab's breakdown ensued immediately following the debonding of the GFRP bars, which intercepted the diagonal shear fractures. The replacement percent of 40% (2 from 5 bars) enhanced the slab flexural resistance, resulting in a shear failure mode rather than a flexure mode. The slab with a replacement percentage of 20% (NFSG20) presented an intermediate behavior, improving the flexure strength to less than that of the slab (NFSG40). Therefore, the performed shear cracks that appeared at load (86 kN) were less than those detected in the case of 40% replacement. The cracking pattern for the specimens (NFSG20 and NFSG40) is shown in Figures 9 and 10.

### 4.2 Load-deflection behavior

The deflection at the slab center was measured at each load increment throughout the test procedure. Sample deflection was examined at both the service and ultimate load stages. Tan and Zhao [27] suggested that the service load corresponds to about 70–75% of the ultimate load. In the present investigation, the service load for each specimen was determined to be 70% of the ultimate load. The ultimate loads of the specimens were defined as the maximum bearing load, as listed in Table 10.

Typically, during the incremental loading process, several distinct stages were observed. Initially, in the elastic region, the deflection increases steadily at a constant rate. Subsequently, as cracks begin to form and propagate, the deflection rate accelerates, leading to a more rapid increase. This trend persists until the steel reinforcement tension stress reaches its yield point, at which point the slope of the deflection curve diminishes. Finally, the test rounds off when the deflection keeps increasing without any concurrent increase in the applied load.

Figure 11 demonstrates the impact of the percentages varying of GFRP bars on the mid-span load-deflection characteristics. The outcomes of (NFSG20 and NFSG40) specimens are contrasted with NFS, which serves as the control sample (without GFRP bars). Based on the load-deflection curves, it is evident that the three slabs exhibit varying levels of stiffness throughout the elastic zone. Table 11

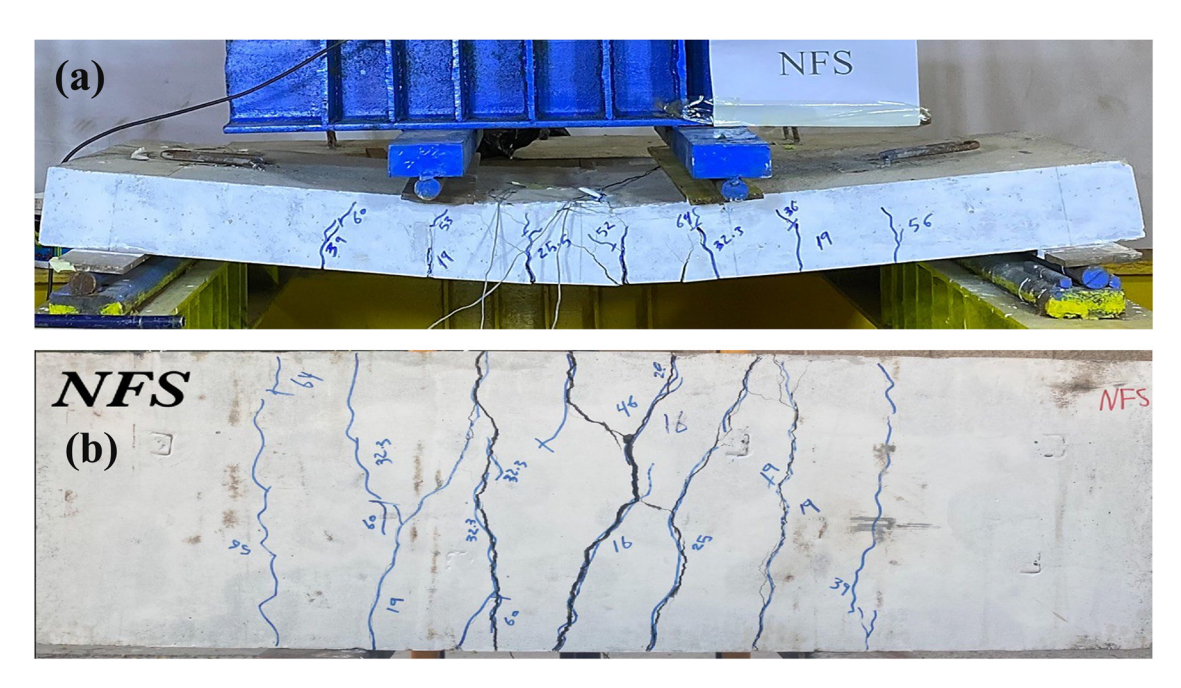


Figure 8: Cracks pattern of the specimen (NFS): (a) side face and (b) bottom face.

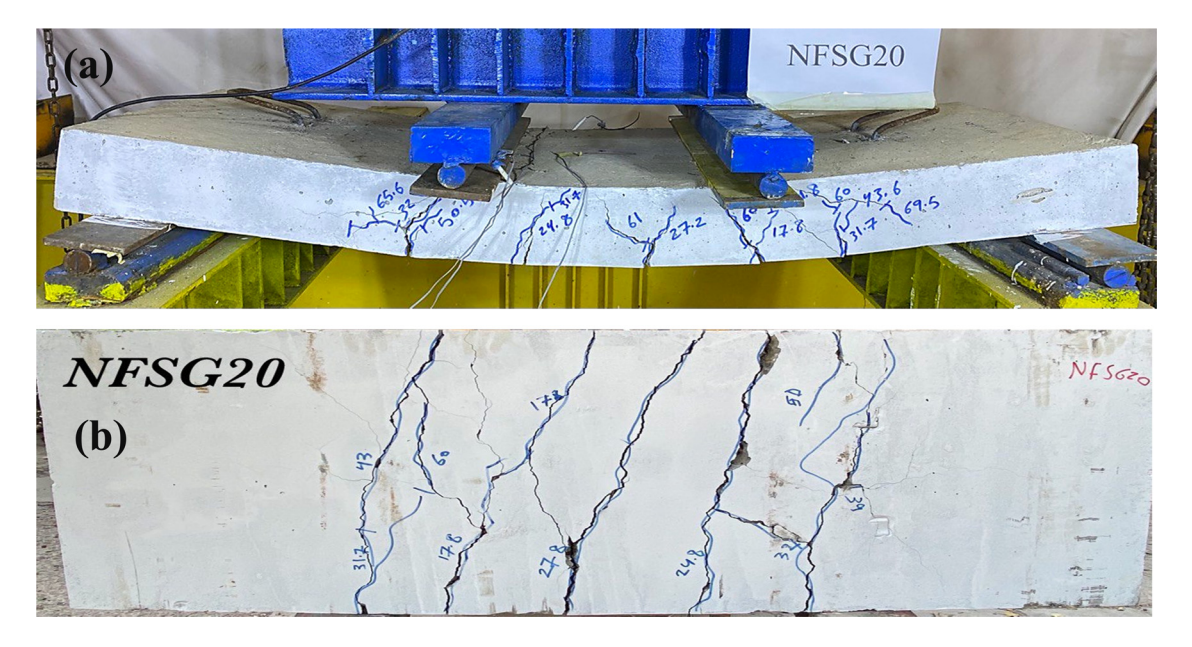


Figure 9: Cracks pattern of the specimen (NFSG20): (a) side face and (b) bottom face.

shows the specimens' stiffness; the results indicated that the stiffness decreased by about 20.32 and 44.04% for the replacement percent of 20 and 40% concerning the reference specimen, respectively.

This discrepancy is attributed to the disparity in the steel and GFRP modulus of elasticity since all the corresponding properties between the tested specimens are compatible, with GFRP possessing a lower modulus of elasticity compared to steel. Compared to steel bars, which

have an approximate modulus of elasticity of 200 GPa, GFRP bars generally have a modulus of elasticity in the 40-75 GPa range. As a consequence, the GFRP-reinforced slab exhibits a reduced initial slope in its load-deflection curve compared to the control slab. These results corroborate the conclusions drawn from the study by Kara et al. [28].

While near the ultimate load, the increasing percentage of steel bars replaced by GFRP bars is directly proportional to the slab strength, or in other words, the deflection

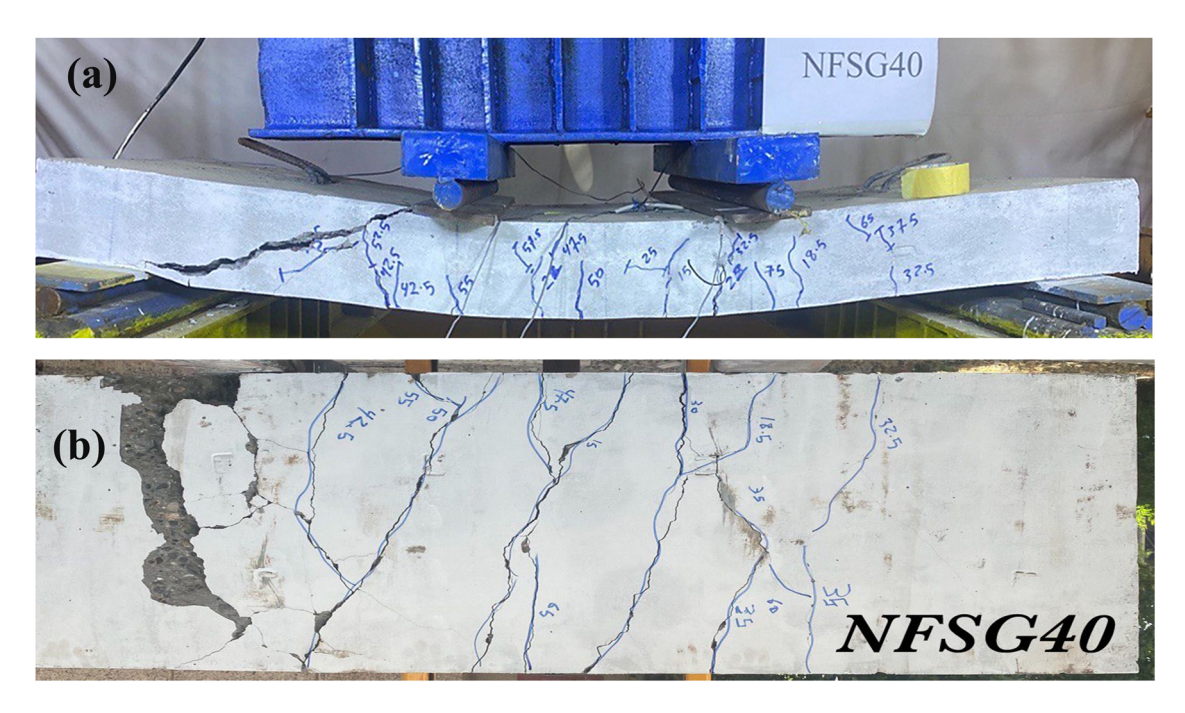
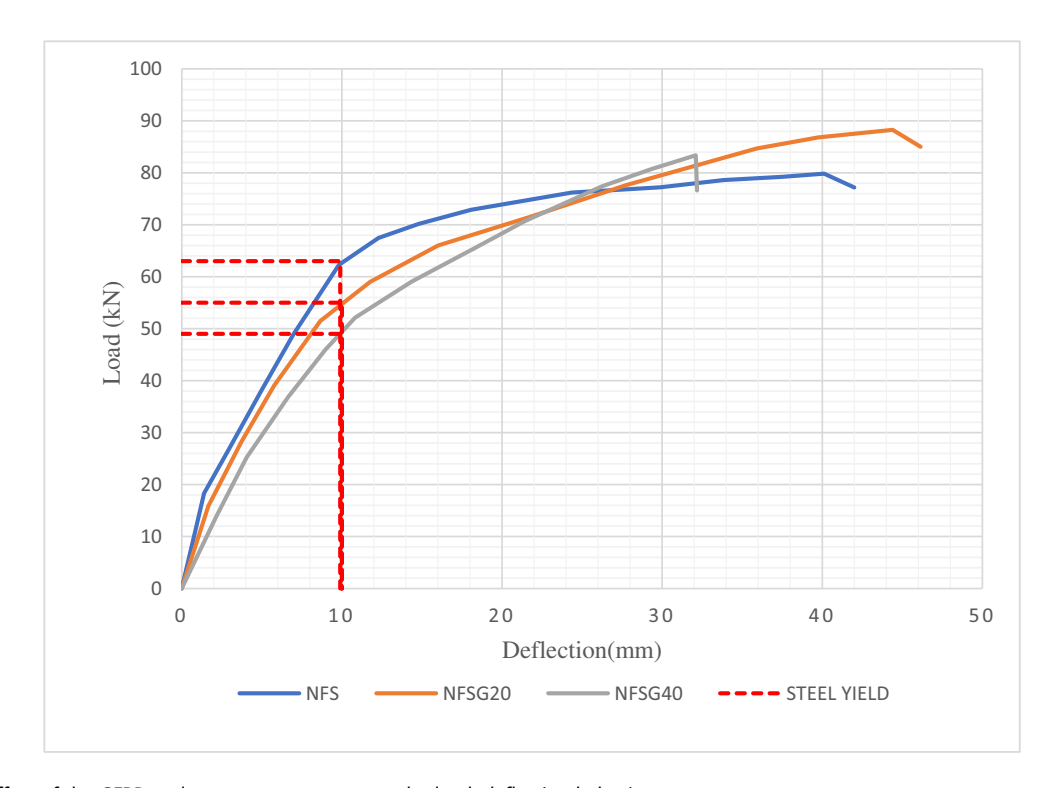


Figure 10: Cracks pattern of the specimen (NFSG40): (a) side face and (b) bottom face.



 $\textbf{Figure 11:} \ \textbf{Effect of the GFRP replacement percentage on the load-deflection behavior.}$ 

decreases at the same load level. However, at service load, the central deflection increased by about 55 and 67% for the replacement percent of 20 and 40% concerning the reference specimen, respectively. While at the ultimate

load of the reference specimen, *i.e.*, 79.62 kN, the central deflection decreased by about 25 and 29% for the replacement percent of 20 and 40% concerning the reference specimen, respectively, as illustrated in Table 12.

Table 11: Stiffness of the tested specimens at cracking load

Specimens	Cracking load (kN)	Deflection at cracking load (mm)	Stiffness, K = P/\(\Delta\) (kN/mm)	Decreasing in stiffness (%)
NFS	19	1.7	11.17	_
NFSG20	17.8	2	8.9	20.32
NFSG40	15	2.4	6.25	44.07

### 4.3 Load-strain relation

The strain-load relations of the reinforced steel bar, GFRP bar, and concrete top surface were measured at the midspan location. Figures 12 and 13 show the influence of increasing the GFRP replacement percentage on the loadstrain relations of flexural steel reinforcement and top concrete surface at mid-span, respectively, for specimens NFS, NFSG20, and NFSG40. The influence of the GFRP replacement ratio was not significant in the elastic range, but it became more noticeable as the response reached the yielding stage of steel reinforcement. Moreover, it was observed that as the replacement percent increased, steel bars reached the yield point earlier. These can be interrupted by the low GFRP modulus of elasticity compared to steel bars. Figure 14 shows the influence of increasing the percentage of steel bars replaced by GFRP bars on the load-strain relations of GFRP bars at mid-span for specimens NFSG20 and NFSG40, respectively.

The flexural steel strain for specimens (NFS, NFSG20, and NFSG40) was 17335.6, 15947.3, and 10882.9 micro-strain, respectively, and GFRP bar's strain was 18080.8 and 13931.9 micro-strain for the NFSG20 and NFSG40 specimens, respectively.

At the ultimate load, the compressive strain in the concrete was measured as follows: 2447 micro-strain for the NFS specimen, 2966 micro-strain for the NFSG20 specimen, and 2578 micro-strain for the NFSG40 specimen. Nonetheless, for specimens NFS, NFSG20, and NFSG40, the concrete compressive strain at the elastic zone was 743.95, 1024.39, and 1264.4, respectively. It is evident that if GFRP is changed, the strain in the concrete increases. This is because GFRP has a lower modulus of elasticity than steel, which causes a decrease in the material's Stiffness and an increase in the amount of deflection that happens within the elastic zone.

The material's stiffness was significantly reduced upon replacing 40% of it. This decrease caused the concrete in the elastic zone to deteriorate and increased strain. Furthermore, the replacement caused a reduction in ductility, which had a significant effect and ultimately led to an early shear failure.

Specimens	specimens Deflection at service load (mm)	% Increase in deflection at service load	Deflection at ultimate load of ref. specimen (79.62 kN)	Deflection at ultimate load of % Decrease in deflection at the ref. specimen (79.62 kN) ultimate load of ref. specimen (79.62 kN)	Deflection at ultimate load (mm)	Deflection at ultimate % Changing in deflection load (mm) at ultimate load
NFS	8.5	Ref.	40.11	Ref.	40.11	Ref.
NFSG20	13.2	55	30	25	44.28	+9.4
NFSG40	14.2	29	28.5	29	32.18	-19.7

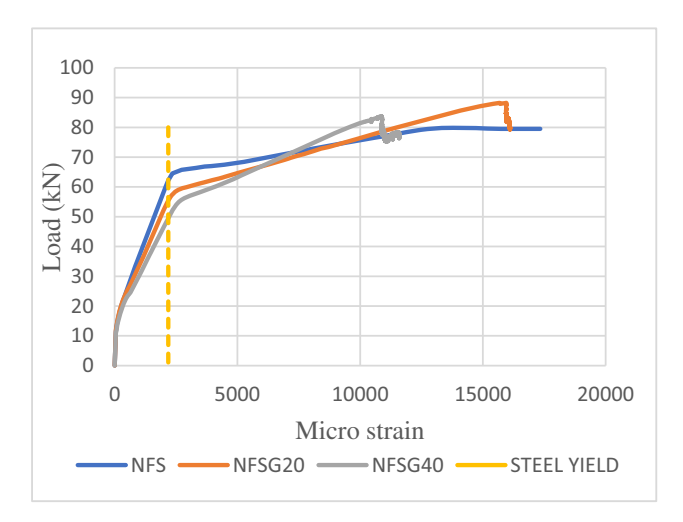


**Figure 12:** Load–strain curves for flexural steel reinforcement at mid-span.

# 4.4 Ductility factor

The ductility index describes a structural element's ability to endure considerable deformation. In other words, it measures the proportion of the central deflection at the point of ultimate load to the central deflection at the first sign of yielding in tension steel bars. Table 13 presents a visual representation of the GFRP substituted percentages varying impact on the ductility factor for specimens NFS, NFSG20, and NFSG40. It was detected that the replacement percent (20%) increased the ductility by 9.13%, while the replacement percent (40%) decreased the ductility by 21%. This result confirms the conclusion of the study by Thamrin *et al.* [29], which states that the capacity increases with the hybrid reinforcement ratio but at the expense of

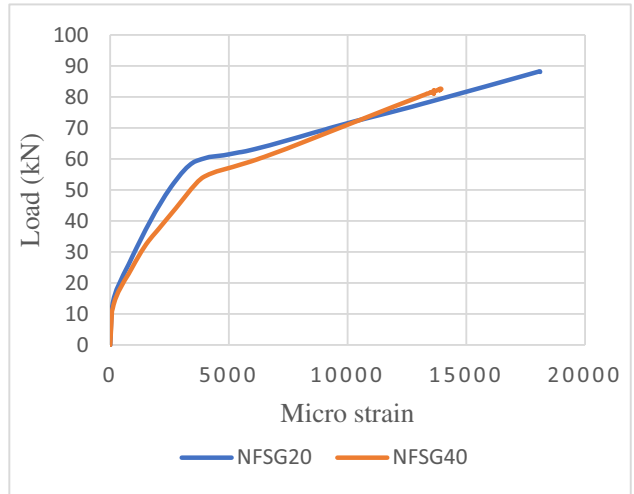


Figure 14: Load-strain curves for concrete top fiber at mid-span.

ductility, which decreases as the hybrid reinforcement ratio increases.

### 4.5 Toughness

Flexural toughness, also known as total absorbed energy, was determined in this study by computing the load—deflection curves integral to the slabs. The term "flexural toughness" pertains to the overall capacity of a material to absorb energy. The energy storage capacity of a loaded concrete structure is a significant characteristic in the field of concrete structures. The absorbed energy, which is quantified by the area under the load—deflection curve, is influenced by both the highest load magnitude and the

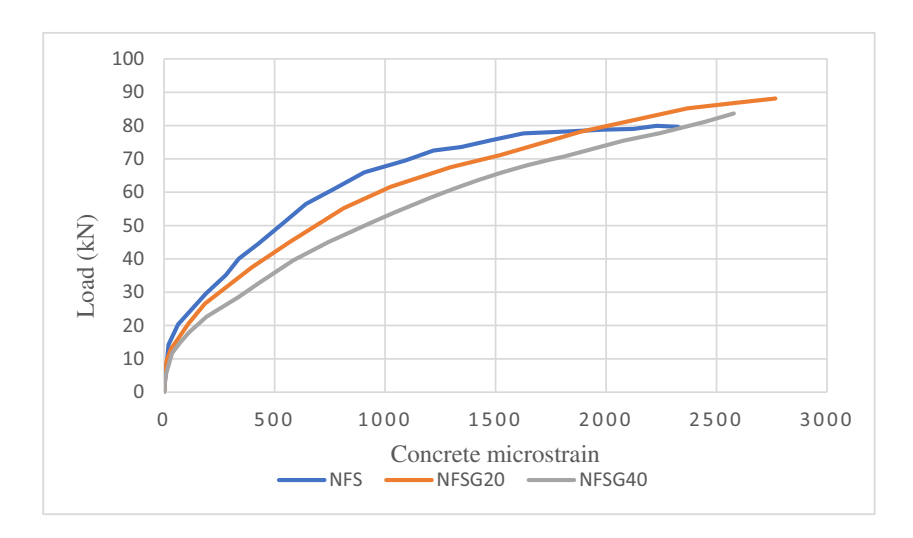


Figure 13: Load-strain curves for GFRP bar at mid-span.

deflection seen at the point of failure. Table 14 shows the total absorbed energy of the tested slabs, and Figure 15 shows a comparison of the total energy values of the tested slabs at failure load. It is noticeable that when 20% of steel reinforcement was replaced, the toughness increased by 11.3% due to the increase in deflection and load capacity. The outcomes differed when the replacement percentage was 40%; the toughness decreased by 34.7% due to the ductility and deflection reduction, even though the load capacity was increased by 5%.

# 5 Numerical analysis

The finite element program ABAQUS/CAE 6.14.1/2019 was used to conduct a study about the structural behavior of one-way slabs reinforced with a combination of GFRP and steel bars. This software can solve a wide range of problems, from simple linear analyses to complex nonlinear simulations. The modeling process consisted of several parts. These parts were generated separately; the concrete slab, steel loading plates, and support plates were modeled as three-dimensional 3D eight-node linear brick solid elements titled (C3D8R) as shown in Figure 16, while the flexural steel reinforcement bars (longitudinal and transverse reinforcement) of the slabs were treated as two-node beam element (B31) and the flexural GFRP reinforcement bars (longitudinal reinforcement) of the slabs were treated as three-dimensional 3D two-node truss element (T3D2) as shown in Figure 17.

Table 13: Ductility factor for the tested specimens

Specimens	Yielding load for steel (kN)	Deflection at steel yield (mm)	Deflection at ultimate load (mm)	Ductility factor
NFS	63	9.9	40.11	4.05
NFSG20	55	10	44.28	4.42
NFSG40	49	10	32.18	3.21

Ductility factor = deflection at ultimate load/deflection at steel yielding.

Table 15 shows how the required plasticity parameters in the current model were set to their default values in ABAQUS (User's Guide, 2014) [30].

Then, interactions between the specimen's parts were chosen; the steel-reinforcement elements (longitudinal and transverse reinforcement) and GFRP-reinforcement elements were connected to the concrete slab elements using embedded constraints, as shown in Figure 18. The concrete slab was considered as a host element, and the steel and GFRP reinforcement were considered as embedded elements. Multiple mesh sizes were adopted in the FEA to get satisfactory and optimal outcomes. This resulted in obtaining negligible differences between adjacent trials; F.E. meshes are illustrated in Figure 19.

A flexural load test was performed on the models in this group. Thus, applied displacement was present in all examples depicted in Figure 20.

# 6 Numerical applications and discussions

### 6.1 Numerical verification

## 6.1.1 Deflection at ultimate load and ultimate load capacity

The nonlinear FEA results were compared to the experimental results of the tested slabs, including the ultimate Load and deflection. Table 16 summarizes the results of the maximum load and deflection. The highest load error limit was less than 2.09%. Furthermore, the comparison shows excellent agreement on the final deflection, with an error range of not more than 7.32%. In the theoretical analysis, the adopted solving process in the ABAQUS software assumes that there is a full interaction between the concrete elements and the steel and GFRP rebar elements, whereas, in the experimental work, this assumption is not exactly applicable, which accounts for the observed percentages of variation between the experimental and theoretical deflection. The experimental and theoretical

Table 14: Toughness of tested slabs

Specimens	Absorbed energy at ultimate load (kN mm)	% Variation of absorbed energy at ultimate load	Absorbed energy at failure load (kN mm)	% Variation of absorbed energy at failure load
NFS	2623.762	_	2771.14	_
NFSG20	2936.207	+11.90	3086.54	+11.38
NFSG40	1802.495	-31.30	1809.15	-34.71

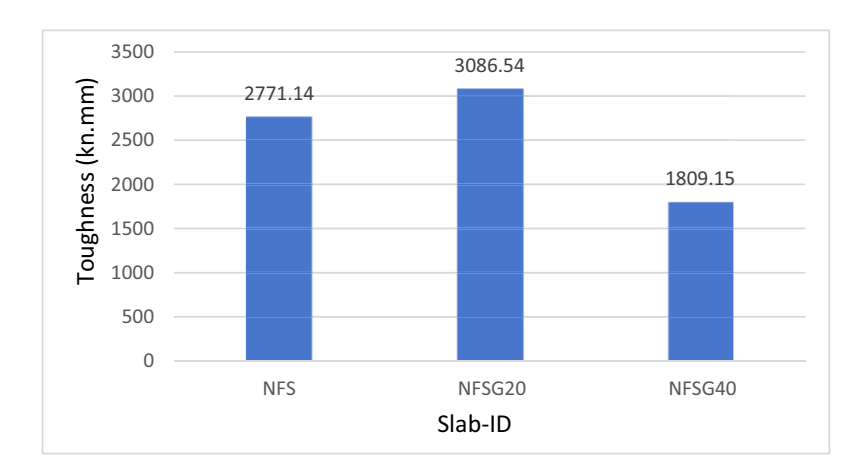


Figure 15: Toughness of the tested slabs.

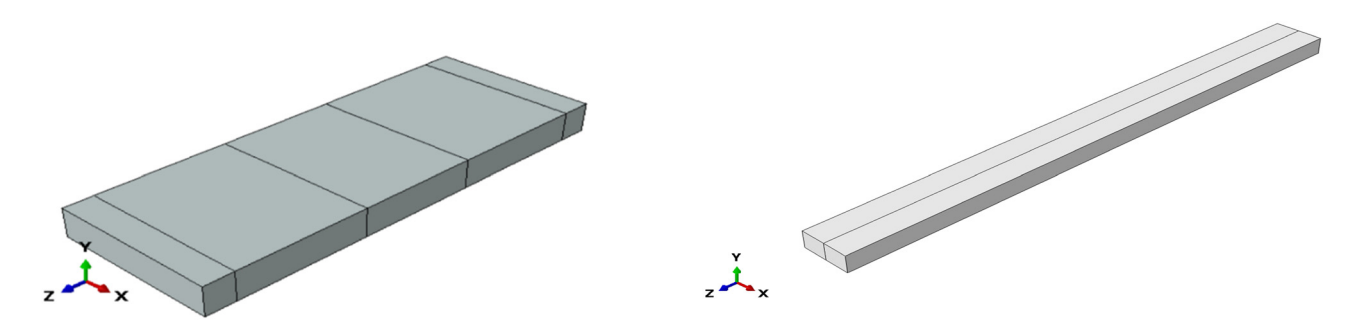


Figure 16: The created parts for the concrete slab and the steel-loading plates.

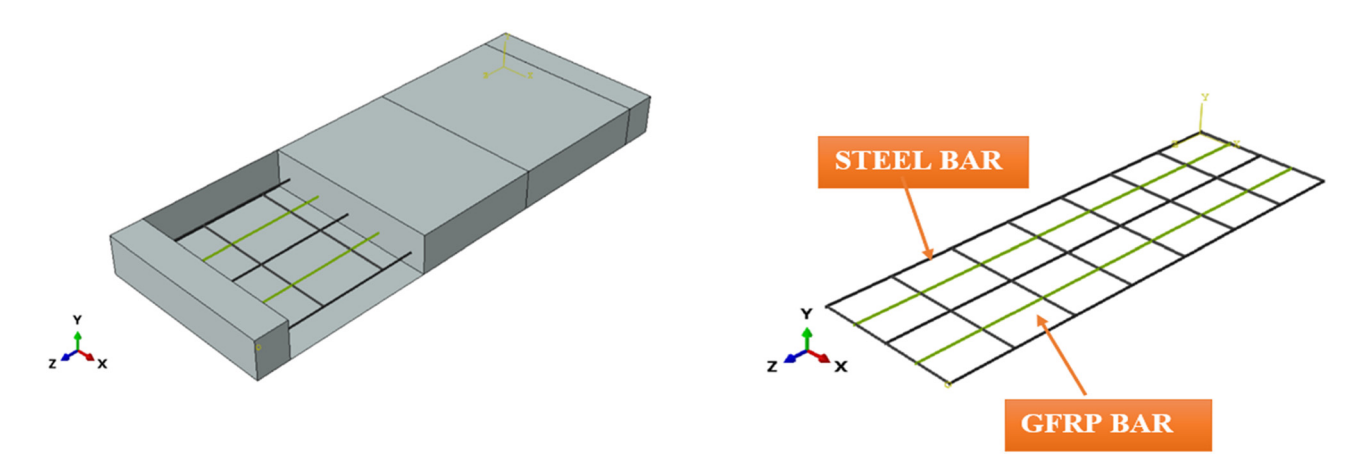


Figure 17: Steel and GFRP rebar.

Table 15: CDPM Parameters adopted in this study

Parameters	ψ	e	$F_{\rm b0}/F_{\rm c0}$	k <sub>c</sub>	μ
Values	45	0.1	1.16	0.6667	0.0001

load-deflection curves in the specimens' middle points are compared in Figures 21–23. The findings of the theoretical analysis, when compared to the experimental work, show an acceptable agreement in the response of the deflection. The load-deflection curves generated theoretically also

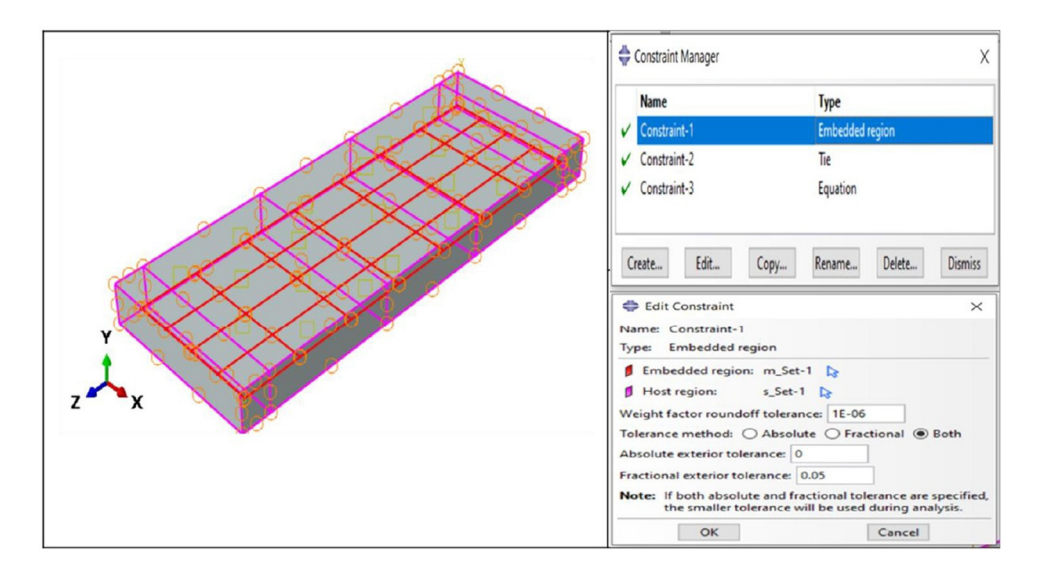


Figure 18: Embedded constraint method for steel and GFRP reinforcement.

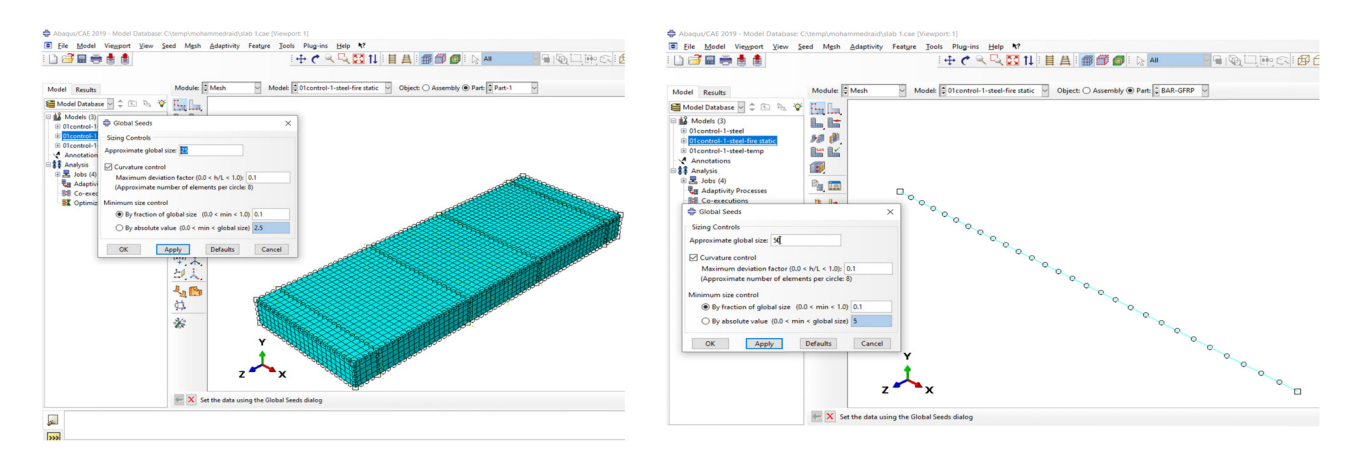


Figure 19: Meshing of the modeled solid slab and meshing of model steel and GFRP reinforcing parts.

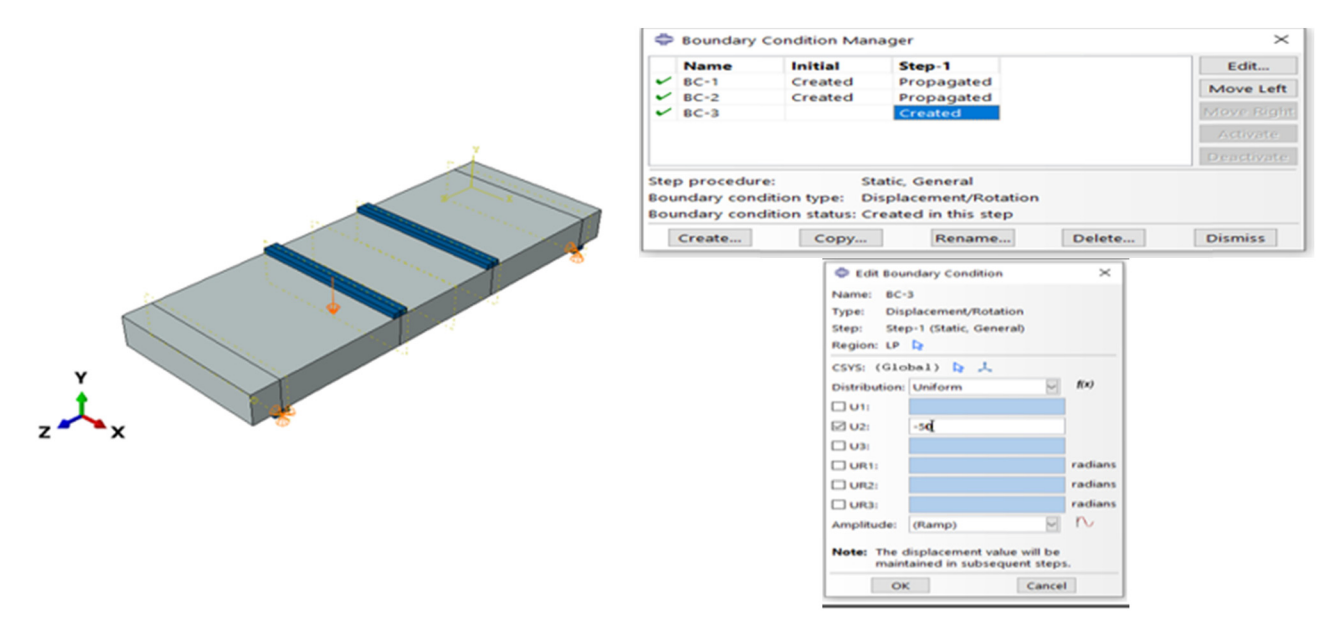


Figure 20: Displacement control application.

show greater uniformity than their experimental curves. The deflection in the elastic zone for the numerical curve is observed to be less than that of the experimental curve. This difference is attributed to the homogeneity and strong bonding between materials in Abacus; this is one of the assumptions that are taken into consideration by the theoretical analysis, which also assumes that the components are homogeneous and that there is a full connection between the concrete and the reinforcement (GFRP and steel).

### 6.1.2 Crack patterns

ABAQUS software can record the crack pattern at each step of the applied load. Crack patterns in the front face of the specimens modeled obtained from the numerical analysis agreed well with those that occurred in the experimental work after failure, as shown in Figures 24–26.

### 6.2 Parametric study

The use of the finite element model allowed a comprehensive parametric analysis, which further built upon the prior validation of experimental data conducted within this study. The attributes being analyzed are related to the concrete compressive strength.

### 6.2.1 Concrete compressive strength

Concrete compressive strength was considered in the parametric analysis. This adopted investigation changed the concrete's compressive strength throughout all slabs using two different concrete compressive strengths, *i.e.*, 65 and 75 MPa. Figure 27 shows the load–deflection curves for slabs built with two different concrete strengths, specifically 65 and 75 MPa. As a result, the slab specimens' capacity for bearing greater loads was increased as the concrete's

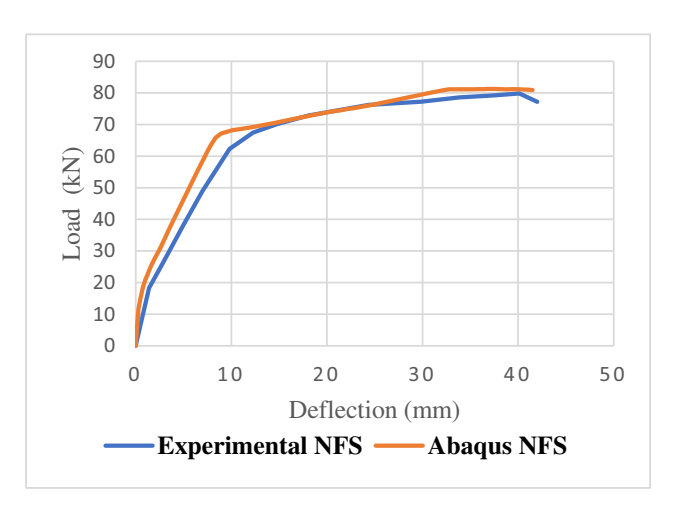
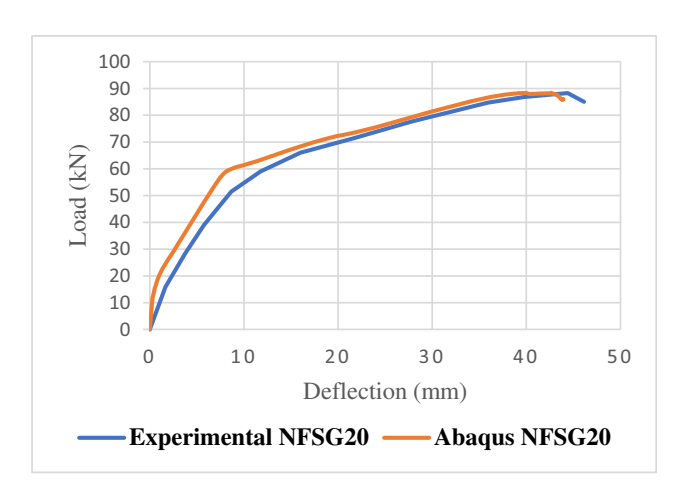


Figure 21: Theoretical and experimental load-deflection curves (NFS).



**Figure 22:** Theoretical and experimental load–deflection curves (NFSG20).

compressive strength increased. As shown in Table 17, concrete compressive strength is directly proportional to the ultimate load value, especially at the 40% replacement percent. Meanwhile, when the concrete compressive strength increased to 65 and 75 MPa, the ultimate load value increased by 19.59 and 21.57%, respectively, compared to the reference

Table 16: Comparison between the results of the experimental and theoretical analysis for ultimate load and deflection

Specimens	Experimental result		FEA		Ratio	
	P <sub>u</sub> (kN)	Δ <sub>u</sub> (mm)	P <sub>u</sub> (kN)	Δ <sub>u</sub> (mm)	$\left  \frac{P_{\mathbf{u}} \operatorname{Exp} - P_{\mathbf{u}} \operatorname{FE}}{P_{\mathbf{u}} \operatorname{Exp}} \right  \%$	$\left  \frac{\Delta_{\mathbf{u}} \operatorname{Exp} - \Delta_{\mathbf{u}} \operatorname{FE}}{\Delta_{\mathbf{u}} \operatorname{Exp}} \right  \%$
NFS	79.62	40.11	81.29	37.17	2.09	7.32
NFSG20	88.13	44.28	88.36	42.63	0.26	3.72
NFSG40	83.64	32.18	82.89	31.95	0.89	0.71
Average					1.08	3.9

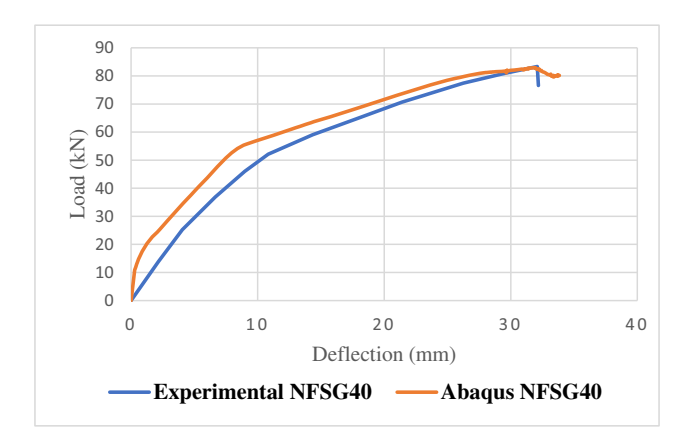


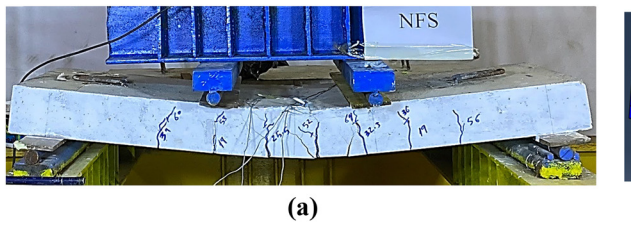
**Figure 23:** Theoretical and experimental load–deflection curves (NFSG40).

specimen. As shown in Figure 28, increasing the compressive strength reduced the shear cracks and changed the failure mode, especially at the 20% replacement percent. In contrast, when the concrete compressive strength increased to 65 and

75 MPa, the failure mode changed from flexural-shear failure to flexural failure.

In contrast to the reference specimen, the comparison revealed that for the specimens with replacement ratios of 20 and 40% and two distinct concrete compressive strengths, *i.e.*, 65 and 75 MPa, the ductility factor had improved by 25.14 and 15.0% for compressive strength of 65 MPa, respectively. In contrast to the reference specimen, the percentages of improved compressive strength of 75 MPa were approximately 35.31 and 19.51%, as indicated in Table 10. Comparing specimens NFSG20 and NFSG40 to the reference specimen, the flexural toughness (absorbed energy) increased by 10.63 and 6.70% at compressive strength of 65 MPa and by 26.47 and 10.29% at compressive strength of 75 MPa, respectively.

The specimens with the replacement percentage of 20% of GFRP had the best flexural toughness and ductility factor concerning the employed parameter (concrete compressive strengths, 65 and 75 MPa); for the ultimate load, the specimens with the replacement percentage of 40% of GFRP had the best percentage.



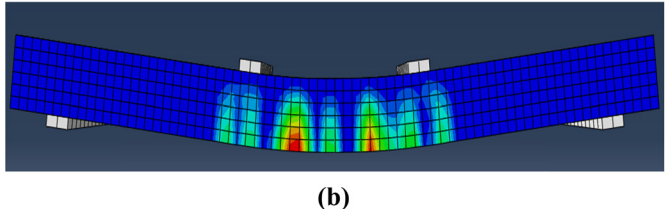
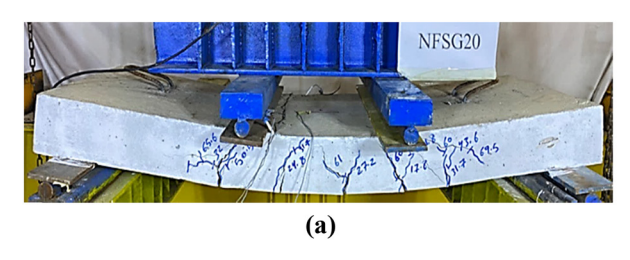


Figure 24: Cracks pattern for the specimen (NFS). (a) Experimental and (b) FE analysis.



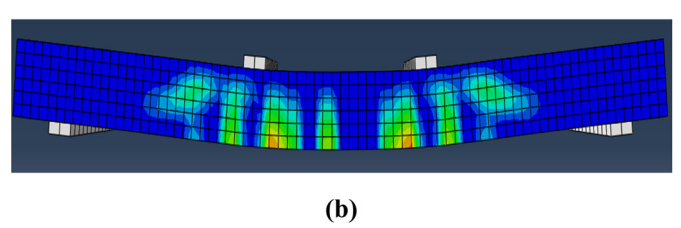
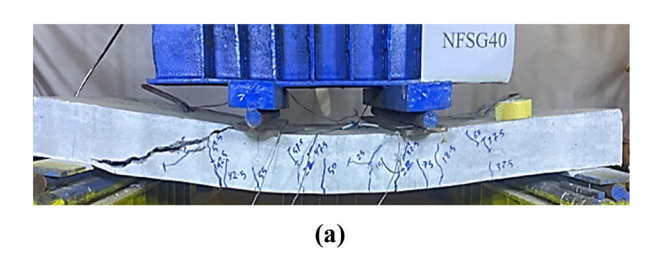


Figure 25: Cracks pattern for the specimen (NFSG20). (a) Experimental and (b) FE analysis.



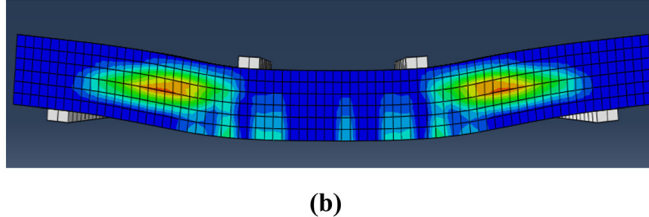
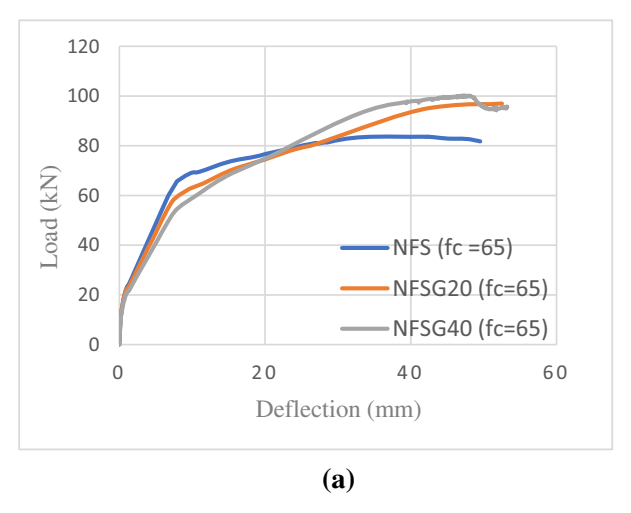
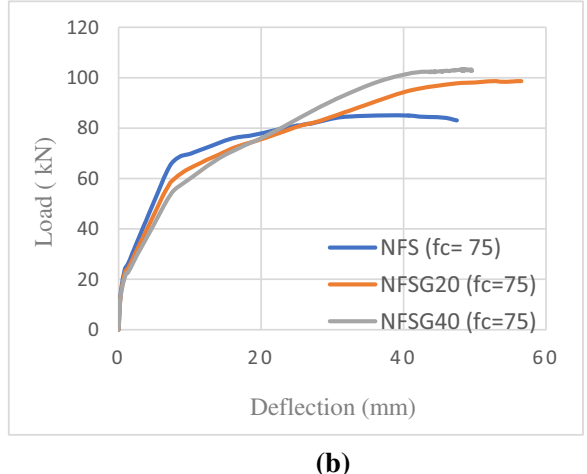


Figure 26: Cracks pattern for the specimen (NFSG40). (a) Experimental and (b) FE analysis.





**Figure 27:** The relationship between load and deflection for concrete of varying strengths is shown in (a) with  $f_c' = 65$  MPa and (b) with  $f_c' = 75$  MPa.

# 7 Conclusions

Several experiments were conducted on three reinforced concrete slabs to evaluate their structural performance. The collected data were further analyzed in conjunction with data from parametric investigations, which included various hybrid reinforcement ratios and placements. Multiple conclusions can be derived from the findings of this investigation:

- 1. Considering the first flexural crack, GFRP bars significantly affected the cracking load reduction; increasing GFRP bars replacement decreased the cracking load by about 6.3 and 21% for the replacement percent of 20 and 40%, respectively, concerning the reference specimen.
- 2. It was observed that the reference slab (NFS) had a flexural failure mode since no inclined cracks were

- found near the supports toward the applied load, and most of the fractures were found in the central third of the slab.
- 3. The replacement percentage of 20% presented an intermediate structural response, and the flexure strength was less than that of 40%. Therefore, the performed shear cracks were less than those detected in the case of 40% replacement.
- 4. The slab with a replacement percentage of 40% collapsed immediately after the GFRP bars deboning that intersected the diagonal shear fractures. This replacement (two of five bars) strengthened the flexural resistance of the slab, resulting in the slab failing with shear mode and also reducing the ductility.
- 5. An increase in the central deflection at the service load was detected by about 55 and 67% for the replacement

Table 17: Outcomes of the theoretical analysis for the considered concrete compressive strength

Specimen designation	P <sub>u</sub> (kN)	Increasing in <i>P</i> <sub>u</sub> (%)	∆ <sub>u</sub> (mm)	Yielding load for steel (kN)	Deflection at steel yield (mm)	Ductility factor	Absorbed energy at failure load (kN mm)
<i>f</i> <sub>c</sub> ′ = 43 MPa							
NFS	81.29	_	37.17	64.3	8.25	4.50	2854.52
NFSG20	88.36	8.69	42.63	58	7.89	5.40	3055.808
NFSG40	82.89	1.96	31.95	52	7.92	4.03	2113.741
$f_{c}' = 65  \text{MPa}$							
NFS	83.69	_	42.1922	65.7	7.91	5.33	3619.507
NFSG20	96.76	15.61	49.6819	58.32	7.44	6.67	4004.564
NFSG40	100.09	19.59	47.303	53.1	7.71	6.13	3862.039
<i>f</i> <sub>c</sub> ′ = 75 MPa							
NFS	85.07	_	40.6864	66.65	7.56	5.38	3519.747
NFSG20	98.66	15.97	56.1531	60.02	7.71	7.28	4451.707
NFSG40	103.42	21.57	48.158	54.22	7.48	6.43	3882.202

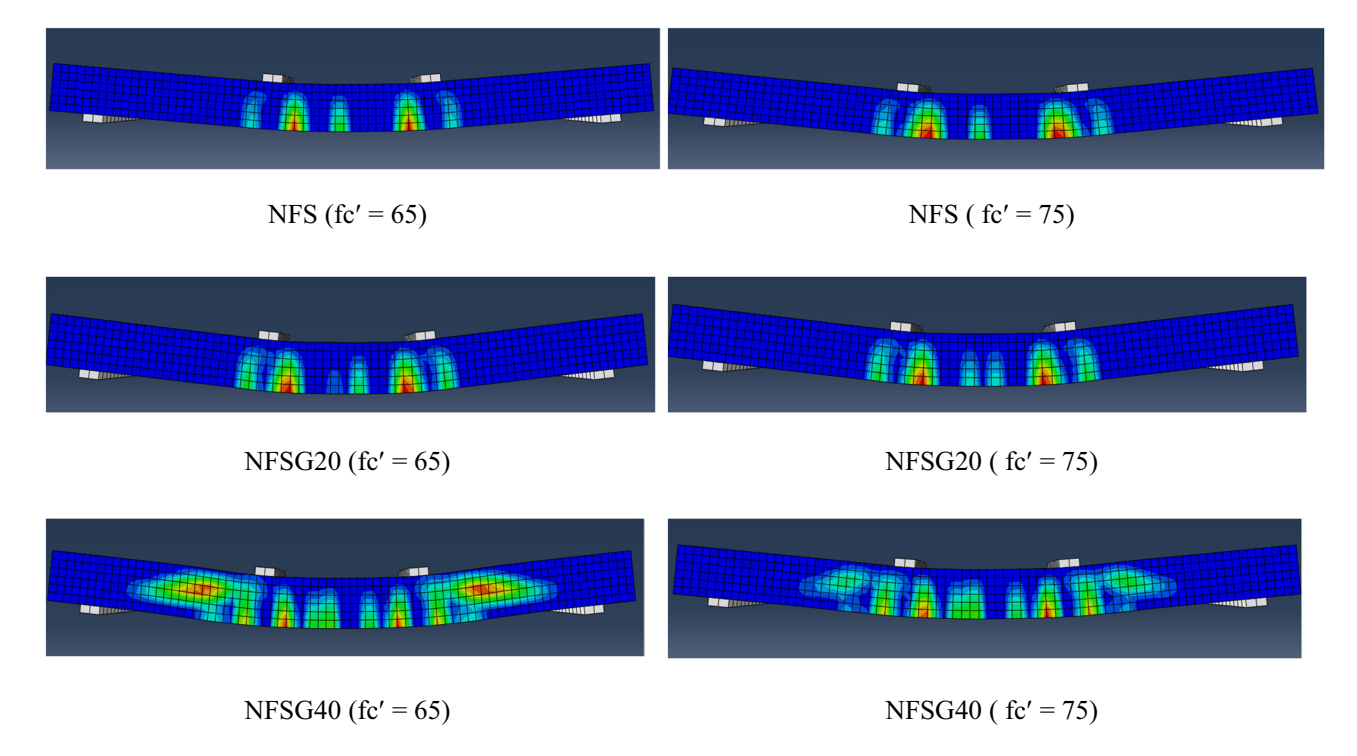


**Figure 28:** The slabs with  $f_c' = 65$  MPa and  $f_c' = 75$  MPa all failed numerically.

percent of 20 and 40% concerning the reference specimen, respectively.

- 6. The fact that GFRP bars have a lower modulus of elasticity than steel bars is largely blamed for the reduction in GFRP-reinforced slab stiffness. GFRP bars typically have an elastic modulus between 40 and 75 GPa, compared to 200 GPa for steel bars. Because of this, they are using GFRP bars as reinforcement to reduce the slab's stiffness or resistance to deflection.
- 7. In the elastic zone, it was observed that the slab stiffness is inversely proportional to the replacement percent. Steel bars reach the yield point earlier since the steel modulus of elasticity is higher than the GFRP.
- 8. Replacement percent of GFRP affected the ductility significantly; an improvement outcome was detected as the replacement was low (20%), while a reduction was observed when the replacement increased to (40%). The same trend was detected for the toughness.
- 9. As concrete compressive strength increases, the ultimate load value increases, especially at the 40% replacement percent; as the concrete compressive strength increased to 65 and 75 MPa, the ultimate load value increased by 19.59 and 21.57%, respectively, compared to the reference specimen of 43 MPa.
- 10. Shear cracks were decreased, and the failure mode was changed when the concrete compressive strength increased, especially at the replacement percent 20%;

- while increasing concrete compressive strength to 65 and 75 MPa, the failure mode changed from flexuralshear failure to flexural failure.
- 11. Improvements can be made in three aspects of the script. First, for the experimental work, it is recommended that full-scale specimens be considered for more significant outcomes. The second recommendation is related to the numerical model. When compressive strength increases, studying the first flexural crack to extract stiffness in the elastic region is suggested. The third recommendation is associated with the numerical model as well. The contact model type between GFRP and steel reinforcement with concrete material can be modeled as a contact surface type instead of an impeded region to investigate the influence of the slipping effect on the resulting efficiency.

Acknowledgment: The author is grateful to the staff in the Civil Department at the Engineering College, Baghdad University.

Funding information: The authors state no funding is involved.

Author contributions: All authors have accepted responsibility for the entire content of this manuscript and approved its submission.

**Conflict of interest:** The authors state no conflict of interest.

**Data availability statement:** Data sharing is not applicable to this article as no datasets were generated or analysed during the current study.

### References

- [1] Jalil A, Al-Zuhairi AH. The behavior of post-tensioned concrete girders subject to partially strand damage and strengthened by NSM-CFRP composites. Civ Eng J. 2022;8(7):1507–21.
- [2] Abdulkareem BF, Izzat AF. Serviceability of post-fire R.C. rafters with openings of different sizes and shapes. J Eng. 2022;28(1):19–32.
- [3] Abbas HQ, Al-Zuhairi AH. Usage of EB-CFRP for improved flexural capacity of unbonded post-tensioned concrete members exposed to partially damaged strands. Civ Eng J. 2022;8(6):1288–303.
- [4] Tuma NK, Al-Ahmed AH, Al-Farttoosi MH. The shear strengthening of reinforced concrete beams was embedded through a section technique-analytical study. IOP Conf Ser: Mater Sci Eng. 2022;888(1):012039.
- [5] Jabbar SAA, Farid SBH. Replacement of steel rebars by GFRP in concrete structures. Karbala Int J Mod Sci. 2018;4:216–77.
- [6] Hassan A, Khairallah F, Mamdouh H, Kamal M. Structural behavior of self-compacting concrete columns reinforced by steel and glass fiber-reinforced polymer rebars under eccentric loads. Eng Struct. 2019;188:717–28.
- [7] Said AI, Abbas OM. Serviceability behavior of high strength concrete I-beams reinforced with carbon fiber reinforced polymer bars. J Eng. 2023;19(11):1515–30. doi: 10.31026/j.eng.2013.11.10
- [8] Ali SI, Allawi AA. Effect of web stiffeners on the flexural behavior of composite GFRP-concrete beam under impact load. J Eng. 2021 Mar;27(3):73–92.
- [9] Al-Ahmed AHA, Al-Jburi MHM. Behavior of reinforced concrete deep beams strengthened with carbon fiber reinforced polymer strips. J Eng. 2016;22(8):37–53.
- [10] El-Hassan H, El Maaddawy T. Microstructure characteristics of GFRP reinforcing bars in harsh environment. Adv Mater Sci Eng. 2019;2019:8053843.
- [11] Benmokrane B, Chaallal O, Masmoudi R. Glass fiber reinforced plastic (GFRP) rebars for concrete structures. Constr Build Mater. 2016:9:353–64.
- [12] El Zareef AM, El Madawy EM. Effect of glass-fiber rods on the ductile behavior of reinforced concrete beam. Alex Eng J. 2018;57(4):4071–9.
- [13] Toutanji HA, Saafi M. Flexural behavior of concrete beams reinforced with glass fiber-reinforced polymer (GFRP) bars. ACI Struct J. 2000;97:712–9.

- [14] Saikia B, Kumar P, Thomas J, Rao KN. Strength and serviceability performance of beams reinforced with GFRP bars in flexure. Constr Build Mater. 2007;21(8):1709–19.
- [15] Jianmin Z, Xiaofeng W, Wanli G, Ying G, Yong Z, Shou C. Experiment and theoretical research on flexural behavior of R.C. slab with highstrength bars. Chin Q Mech. 2011;32(14):626–33.
- [16] Qu W, Zhang X, Huang H. Flexural behavior of concrete beams reinforced with hybrid (GFRP and steel) bars. J Compos Constr. 2009;13(5):350–9.
- [17] Barris C, Torres L, Comas J, Miàs C. Cracking and deflections in GFRP RC beams: An experimental study. Compos Part B Eng. 2013;55(12):580–90.
- [18] Chang K, Seo D. Behavior of one-way concrete slabs reinforced with GFRP bars. J Asian Archit Build Eng. 2012;11(2):351–8.
- [19] Sadraie H, Khaloo A, Soltani H. Dynamic performance of concrete slabs reinforced with steel and GFRP bars under impact loading. Eng Struct. 2019;191:62–81.
- [20] Al-Rubaye M, Manalo A, Alajarmeh O, Ferdous W, Lokuge W, Benmokrane B, et al. Flexural behavior of concrete slabs reinforced with GFRP bars and hollow composite reinforcing systems.". Composite Struct. 2020;236:111836.
- [21] Adam MA, Erfan AM, Habib FA, El-Sayed TA. Structural behavior of high-strength concrete slabs reinforced with GFRP bars. Polymers. 2021;13(17):2997.
- [22] Golham MA, Al-Ahmed AHA. Behavior of GFRP reinforced concrete slabs with openings strengthened by CFRP strips. Results Eng. 2023;18:101033.
- [23] IQS 5-2019. Iraq Standard Specification for Portland Cement. 2019.
- [24] IQS 45-1993. Aggregate from Natural Sources for Concrete and Building Construction. 1993.
- [25] ASTM standard A 615/A 615M,15a. Standard specification for deformed and plain carbon-steel bars for concrete reinforcement. West Conshohocken, PA, USA: ASTM International; July 2015.
- [26] ACI Committee 318. Building code requirements for structural concrete (ACI 318-19) and commentary (ACI 318R-19). Farmington Hills: American Concrete Institute; 2019. p. 623.
- [27] Tan KH, Zhao H. Strengthening of openings in one-way reinforced-concrete slabs using carbon fiberreinforced polymer system. J Compos Constr. ASCE, October. 2004;8(5):393–402.
- [28] Kara IF, Ashour AF, Köroğlu MA. Flexural behavior of hybrid FRP/ steel reinforced concrete beams. Composite Struct. 2015;129:111–21.
- [29] Thamrin R, Zaidir Z, Iwanda D. Ductility estimation for flexural concrete beams longitudinally reinforced with hybrid FRP–steel bars. Polymers. 2022;14(5):1017.
- [30] Abaqus Analysis User's Guide. Vol. IV: Elements. Waltham, Massachusetts, USA: Dassault Systems; 2014.